Chemical bond overlap descriptors from multiconfiguration wavefunctions

Carlos V. Santos-Jr.[†] and Renaldo T. Moura Jr.[*,‡,¶]

†*Department of Chemistry*
Federal University of Paraiba, Joao Pessoa, PB 58051-970, Brazil
‡*Department of Chemistry and Physics*
Center of Agrarian Sciences, Federal University of Paraiba, Areia, PB 58397-000, Brazil
¶*Computational and Theoretical Chemistry Group (CATCO)*
Department of Chemistry, Southern Methodist University Dallas, TX 75275, USA

E-mail: renaldo.mourajr@cca.ufpb.br

Abstract

Chemical bonds are fundamental in chemistry, serving as the foundation for understanding molecular properties. Over time, various theories and descriptors have evolved to characterize these bonds since the inception of quantum mechanics. This report focuses on extending overlap density and its topological descriptors (OP/TOP) using Multiconfigurational Self-Consistent Field (MCSCF) wavefunctions, highlighting their importance. We present a comparative analysis of OP/TOP descriptors using CASSCF and DCD-CAS(2) wavefunctions for a diverse range of molecular systems, including X−O bonds in X−OH (where X = H, Li, Na, H_2B, H_3C, H_2N, HO, F) and Li−X' (where X' = F, Cl, and Br) molecular test systems. CAS(10,16) and CAS(6,20) calculations challenge the MCSCF-based OP/TOP bond descriptors, with comparisons to QTAIM and LVM descriptors. Additionally, we examine the Li–F dissociation profile using OP/TOP descriptors. Our study reveals that chemical bonds formed between atoms with varying electronegativities exhibit overlap density shifted towards the more electronegative atom, as predicted by the OP/TOP descriptors. Quantitative assessments using critical point overlap density and its Laplacian descriptors show reduced spreading in bonds with increasing electronegativity differences. The sensitivity of OP/TOP descriptors to ionic/neutral inversion during Li–F dissociation showcased their potential in elucidating intricate bond phenomena. These insights into multiconfigurational wavefunctions, facilitated by OP/TOP descriptors, open new avenues for understanding chemical bond dynamics across multiconfigurational and multireference wavefunction classes, offering novel applications in the field of chemistry.

Introduction

Chemical bonds represent a fundamental and pervasive concept in chemistry, providing an intrinsic foundation that assists chemists in comprehending the properties and characteristics of molecules and materials. Since the inception of quantum mechanics,[1–4] a multitude of theories have arisen to model and characterize the nature of chemical bonds, resulting in the development of diverse chemical bond descriptors from various perspectives. Some of the most renowned approaches for analyzing chemical bonds can be broadly categorized into two groups. The first group includes energy-based decomposition descriptors, such as Bond Dissociation Energy (BDE), Energy Decomposition Analysis (EDA),[5–7] the Acti-

https://doi.org/10.26434/chemrxiv-2023-70tx9 ORCID: https://orcid.org/0000-0002-8151-1640

vation Strain Model (ASM),[8] and the Local Vibrational Mode (LVM) theory.[9–12] The second group comprises methods based on wavefunction or electron density analysis, such as the Quantum Theory of Atoms in Molecules (QTAIM),[13] the Electron Localization Function (ELF)[14] and the Electron Localizability Indicator (ELI-D), as well as Natural Bond Orbitals (NBOs) analysis.[15]

A new set of density-based decomposition chemical bond descriptors, as part of the Chemical Bond Overlap (OP) model, was recently introduced.[16] The OP model builds upon overlap properties initially introduced by Malta and colleagues,[17] encompassing a range of chemical bonding descriptors that have been expanded in recent work.[18] This extension includes topological descriptors (TOP) derived from a numerically obtained overlap density through localized molecular orbitals. Originally devised for the analysis of diatomic or diatomic-like systems,[17] the OP model initially found utility in describing Ln−L bonds within lanthanide complexes.[19] Subsequently, it has proven versatile and has been successfully applied to a variety of systems, including diatomics,[20,21] molecular species,[16,22] coordination compounds,[23–25] and solid-state materials.[21,26] An understanding of overlap polarizability is crucial for comprehending the relationship between 4f-4f transition intensities and the covalent character of Ln−L bonds.[25,27–29] Moreover, the OP approach has been effectively employed to describe chemical bonding in organic reaction systems.[22] This application has yielded results in excellent agreement with other chemical bonding analysis models, such as Quantum Theory of Atoms in Molecules (QTAIM)[13] and Local Vibrational Mode (LVM).[9,11]

All of the previously mentioned methods (BDE, EDA, ASM, LVM, QTAIM, ELF, and NBO) provide chemical bond descriptors that are only as accurate as the model chemistry employed to describe the wavefunction or the electron density of the target molecular system. In this context, the simplicity and computational efficiency of Density Functional Theory (DFT) methods and approximations, which implicitly handle electron correlation, may falter when dealing with strong correlation effects, systems featuring a significant mixing of configurations, and other related topics.[30]

Wavefunction theory has long established that not all chemical species can be adequately represented by a single determinant wavefunction. For cases where the electronic state of a molecule cannot be reasonably described by a single Slater determinant, the Complete Active Space (CAS) Self-Consistent Field (CASSCF) method[31] offers a means to account for static electron correlation. The most widely employed post-CASSCF methods for addressing dynamic electron correlation include Complete Active Space Second-Order Perturbation Theory (CASPT2)[32,33] and Second-Order N-Electron Valence State Perturbation Theory (NEVPT2).[34] Given that CASPT2 and NEVPT2 methods retain a frozen 0th-order wavefunction, any chemical bond descriptors employed for analyzing the electron density derived from the wavefunction must rely on the pure CASSCF wavefunction.

This scenario is common in numerous applications of QTAIM across various systems. Typically, QTAIM and other density-based descriptors make use of the CASSCF wavefunction, whereas energy-based descriptors rely on energies (and their first, and second derivatives) corrected using CASPT2 and NEVPT2 methods.

Malček and colleagues[35] explored how QTAIM describes electronic densities in M–M bonds (M = Cu, Cr) within tetrakis complexes, considering both single-determinant methods and CASSCF. Additionally, Li and colleagues[36] provided QTAIM descriptors for M–M (M = B, Al, and Ga) bonds in M_3 clusters, utilizing the CASSCF wavefunction. Their findings revealed the presence of 3-center-2-electron bonds and classified B-B and Al–Al bonds as covalent, while Ga-Ga bonds exhibited metallic behavior. Giricheva and co-authors[37] investigated the nature of the Co–O bond in Gaseous Oxopivalate Cobalt(II) using QTAIM topological descriptors with the CASSCF wavefunction.

Peach and colleagues[38] conducted an investigation into the effects of spin-orbital coupling in astatine diatomic molecules and trihalide anions. Their study revealed that spin-orbital coupling reduces the covalent nature of At–X bonds, where X represents At, I, Br, Cl, or F. Reuther and colleagues[39] introduced a QTAIM-based methodology for predicting the composition of ionic or covalent bonds, employing Valence Bond or CASSCF wave functions. Their study demonstrates the effectiveness of this model on small, well-known molecules. Zabanov and collaborators[40] employed QTAIM to analyze CASSCF wavefunctions in order to investigate chemical bonds in iron and cobalt metal complexes of porphyrazines.

All the aforementioned studies are based on the assumption that dynamic correlation corrections to the wavefunction can be considered negligible, and they perform topological QTAIM analyses using the CASSCF wavefunction. However, it's important to note that dynamic correlation effects can play a significant role in some chemical systems. Addressing this issue, Pathak and colleagues[41] provided a thoughtful discussion on the incorporation of dynamic correlation effects into the 0th-order wavefunction. In their work, they introduced the Dynamic Correlation Dressed Complete Active Space with Second-Order Treatment (DCD-CAS(2)) method. They highlighted the cost-effectiveness and superior performance of this approach when compared to NEVPT2 energies.

In light of the significance of Multiconfigurational Self-Consistent Field (MCSCF) methods for providing a more accurate description of chemical bond descriptors, this report elaborates on the extension of OP/TOP descriptors using MCSCF wavefunctions. Initially, we demonstrate that canonical molecular orbitals yield a consistent representation of the overlap density comparable to that obtained using their localized molecular orbitals counterparts. The implementation is designed to be applicable to any Configuration Interaction (CI) type of wavefunction. However, to showcase this new functionality, we will provide a comparative analysis between OP/TOP descriptors using CASSCF and DCD-CAS(2) wavefunctions. The H_2O molecule serves as a test example for evaluating basis set and active space size convergence, while a set of test examples, as illustrated in Figure 1, are adopted to challenge the MCSCF implementation of OP/TOP bond descriptors reported in this work, and their comparison with QTAIM and LVM descriptors. The targeted bonds in polyatomic molecules were selected from the report by Fugel and colleagues.[42] The dissociation pattern of the Li–F bond was selected to emphasize the differences in OP/TOP descriptors when using the CASSCF and a second-order corrected wavefunction (DCD-CAS(2)).

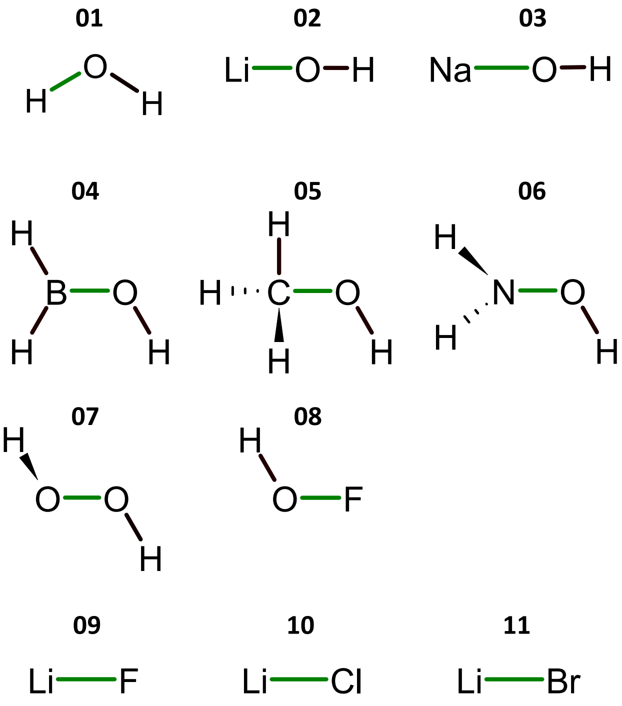

Figure 1: Schematic representation of the studied molecular systems. The examined chemical bonds are highlighted in green.

Methodology

In the methodology section, we will begin by demonstrating that canonical molecular orbitals (MOs) provide a consistent representation of the overlap density comparable to that obtained using their localized Molecular Orbitals (LMOs) counterparts. Subsequently, we will derive the overlap density from a Multiconfigurational Self-Consistent Field wavefunction. Finally, we will delve into the main OP/TOP descriptors.

Overlap density from canonical and localized MOs

The expanded OP model introduced in 2020[43] decomposes a given LMO electron density into atomic (one-center) and overlap (two-center) components. Assuming that the LMO l is associated with a chemical bond A−B in a given molecule, the overlap density at a point $\vec{r}$ in space can be calculated using LMOs with the following expression:

$$\rho_{l,\mathrm{OP}}(\vec{r}) = \sum_{i \in A}^{m} \sum_{j \in B}^{m} c_{li} c_{lj} \phi_{li}(\vec{r}) \phi_{lj}(\vec{r}) \tag{1}$$

Here, ϕ_{li} represents the primitive or contracted functions, c_{li} are the LMO expansion coefficients, and m is the number of basis functions or atomic orbitals. The overlap portion is subsequently employed to compute various chemical bond descriptors, including electron density, Coulomb repulsion, and polarizability, by applying the respective operator within the LMO overlap region. Localization techniques, such as the well-known Pipek-Mezey localization,[44] rely on atomic-charge based methods and may involve various types of charge partitions, including Mulliken, Bader, Becke, Löwdin, or Hirshfeld populations.[45]

It's worth emphasizing that these localization procedures can introduce bias into the overlap density. Therefore, in this study, we opt to directly compute the overlap density using MOs rather than LMOs. To achieve this, for a single Hartree-Fock (HF) or DFT $|\varphi\rangle$ determinant, the total electron density at a point $\vec{r}$ in space is computed as follows:

$$\rho_{mol}(\vec{r}) = \langle \varphi \mid \varphi \rangle = \sum_{l}^{M} n_l \sum_{i}^{m} \sum_{j}^{m} c_{li} c_{lj} \phi_{li}(\vec{r}) \phi_{lj}(\vec{r}) \tag{2}$$

In this equation, l ranges over all M MOs (spatial components of spin-orbitals), n_l represents the MO occupancy, m is the number of atomic orbitals (AOs), c_{li} denotes the AOs' expansion coefficients from the Linear Combination of Atomic Orbitals (LCAO), and ϕ_{li} corresponds to the primitive or contracted functions describing the AOs.

Without losing any information, the summations involving i and j in $\rho_{mol}(\vec{r})$ in Equation 2 can be decomposed into one-center and two-center contributions. This decomposition is applicable to an example molecule such as −R−A−B−R'−, where our primary interest lies in the chemical bond A−B, while R and R' represent general molecular fragments. Considering $\rho^{l}_{MO_{ij}}(\vec{r}) = \sum_i^m \sum_j^m c_{li} c_{lj} \phi_{li}(\vec{r}) \phi_{lj}(\vec{r})$, the modified form of Equation 2 is expressed as follows:

$$\begin{aligned} \rho_{mol}(\vec{r}) &= \langle \varphi \mid \varphi \rangle \\ &= \sum_{l}^{M} n_l (\rho^{l}_{MO_{AA}}(\vec{r}) + 2\rho^{l}_{MO_{AB}}(\vec{r}) + \\ &\quad \rho^{l}_{MO_{BB}}(\vec{r}) + \rho^{l}_{MO_{AR}}(\vec{r}) + \rho^{l}_{MO_{BR}}(\vec{r})) \end{aligned} \tag{3}$$

In this equation, $\rho^{l}_{MO_{AA}}(\vec{r})$ and $\rho^{l}_{MO_{BB}}(\vec{r})$ represent the one-center terms (with $i \in A$ and $j \in A$), and $\rho^{l}_{MO_{AB}}(\vec{r})$ is the two-center (overlap) term (with $i \in A$ and $j \in B$) of the l-th MO contribution to the total electron density. Terms $\rho^{l}_{MO_{AR}}(\vec{r})$ and $\rho^{l}_{MO_{BR}}(\vec{r})$ account for the contributions of the remaining atoms in the molecule, which include other one-center and two-center terms. Since we are specifically interested in the A−B bond, its overlap density is expressed for a single determinant as:

$$\rho_{\mathrm{OP}}(\vec{r}) = 2 \sum_{l}^{M} n_l \sum_{i \in A}^{m} \sum_{j \in B}^{m} c_{li} c_{lj} \phi_{li}(\vec{r}) \phi_{lj}(\vec{r}) \tag{4}$$

In this equation, we only consider the two-center terms (when $i \in A$ and $j \in B$). This is referred to as the overlap density ρ_{OP} and is treated numerically.[18]

Overlap density from MCSCF wavefunctions

To obtain OP/TOP descriptors from an MCSCF wavefunction, the first step involves constructing what is referred to in the OP model as the overlap density, ρ_{OP}. To do this, we begin by writing the configuration interaction (CI) expansion for the wavefunction:

$$|\psi\rangle = \sum_k \mathbb{C}_k \cdot |\varphi_k\rangle \tag{5}$$

where $\mathbb{C}_k$ are the CI expansion coefficients, and $|\varphi_k\rangle$ represents different determinants or configurational state functions (CSFs). Taking $|\varphi_0\rangle$ as the Hartree-Fock reference, the configuration interaction with singles and doubles excitations (CISD) wavefunction can be expressed as:

$$|\psi\rangle = \mathbb{C}_0 \cdot |\varphi_0\rangle + \sum_{ra} \mathbb{C}_a^r \cdot |\varphi_a^r\rangle + \sum_{a<b,r<c} \mathbb{C}_{ab}^{rs} \cdot |\varphi_{ab}^{rs}\rangle \tag{6}$$

Here, $|\varphi_a^r\rangle$ is the CSF generated when spin-orbital a is replaced by spin-orbital r, and $|\varphi_{ab}^{rs}\rangle$ is the CSF generated when spin-orbitals a and b are replaced by spin-orbitals r and s. The total electron density for the wavefunction expressed by Eq. 6 is written as follows:

$$\langle\psi \mid \psi\rangle = \sum_{ij} \mathbb{C}_i \cdot \mathbb{C}_j \cdot \langle\varphi_i \mid \varphi_j\rangle \tag{7}$$

where a significant number of CSFs must be considered. The matrix elements $\langle\varphi_i \mid \varphi_j\rangle$ involve determinants that can be equal or may differ by one, two, or more spin-orbitals. Using the rules of Slater-Condon[46,47] for matrix elements and considering the unit operator, the evaluation of overlap between $\langle\varphi_i|$ and $|\varphi_j\rangle$ arbitrary determinants formed from the same set of spin-orbitals leads to the matrix elements $\langle\varphi_i \mid \varphi_j\rangle = \delta_{ij}$, being nonzero only for equal determinants.

Assuming a set of orthogonal N-electron functions known as Configuration State Functions (CSFs), the total electron density at position $\vec{r}$ can be expressed as:

$$\langle\psi \mid \psi\rangle = \sum_k \mathbb{C}_k^2 \cdot \langle\varphi_k \mid \varphi_k\rangle \tag{8}$$

Here, $\langle\varphi_k \mid \varphi_k\rangle$ encompasses all CSFs for the MCSCF wavefunction, as described in Eq. 2, where $\mathbb{C}_k$ represents their expansion coefficients. It's important to note that Eq. 8 simplifies to Eq. 2 when considering only one determinant (or CSF), with $\mathbb{C}_k = 1.0$.

Applying the same decomposition as in Eq. 3 and utilizing Eq. 4 for each determinant term $\langle\varphi_k \mid \varphi_k\rangle$, the overlap density takes the following form:

$$\rho_{\mathrm{OP}}(\vec{r}) = 2\sum_k^{\mathrm{CSFs}} \mathbb{C}_k^2 \sum_l^{M_k} n_l \sum_{i\in A}^m \sum_{j\in B}^m c_{li} c_{lj} \phi_{li}(\vec{r}) \phi_{lj}(\vec{r}) \tag{9}$$

Here, $\mathbb{C}_k$ represents the CI expansion coefficients for the k-th CSF. The index l ranges over the M_k molecular orbitals (the spatial part of the spin-orbital) that constitute the k-th CSF, with n_l denoting the occupancy of the l-th MO. $\phi_a(\vec{r})$ and $\phi_b(\vec{r})$ are atomic orbitals evaluated at position $\vec{r}$, while c_{li} and c_{lj} are their respective coefficients. The factor 2 on the right side of Eq. 9 accounts for the possibilities of $(i \in A)(j \in B)$ and $(i \in B)(j \in A)$. In a CASSCF procedure, both $\mathbb{C}_k$ and c_l are adjusted to obtain the total electronic wavefunction with the lowest possible energy.

It should be noted that, by definition, Eq. 9 can be used for any CI expansion, including any multiconfigurational self-consistent field, multireference CI, or full-CI function. The only difference lies in the amount and quality of information that will be passed to our ChemBOS software (www.chembos.website), which already has the functionality to use MCSCF wavefunctions. This functionality is available in a development version that allows the reading of wavefunctions generated in programs like Gaussian and Orca.

The calculation of $\rho_{\mathrm{OP}}(\vec{r})$ involves numerically evaluating the expression given in Eq. 9 at various grid points $\vec{r}$ in space. This calculation selects only the positive (two-center) portion, as explained in our recent report.[18] Furthermore, all numerical integration calculations are conducted using our Adaptive Subspace by Integral Importance (ASII) algorithm,[48] which is integrated into ChemBOS.

OP/TOP descriptors

The central idea of the OP/TOP model is to use $\rho_{\mathrm{OP}}(\vec{r})$ to access descriptors related to the chemical interaction between pairs of atoms. Here, we discuss four OP/TOP descriptors for the MCSCF wavefunction, namely: overlap density ρ_{OP}, intra-overlap Coulomb repulsion $J_{\mathrm{OP}}^{\mathrm{intra}}$, and density $(\rho_{\mathrm{OCP}}^{l}(\vec{r}))$ and Laplacian $(\nabla^2\rho_{\mathrm{OCP}}^{l}(\vec{r}))$ at the overlap critical point. These descriptors have been introduced previously.[16,18]

The **overlap density** ρ_{OP} is determined by integrating Eq. 9 over the positive $\rho_{\mathrm{OP}}(\vec{r})$ values. In our OP model, ρ_{OP} specifically represents the electron density shared between the atoms involved in a bond and is calculated as follows:

$$\begin{aligned}\rho_{\mathrm{OP}} &= \int_{-\infty}^{+\infty} \rho_{\mathrm{OP}}(\vec{r})\, dv \\ &\approx \sum_{\text{3D grid}} 2 \sum_{k}^{\text{CSFs}} \mathbb{C}_k^2 \sum_{l}^{M_k} n_l \sum_{i\in A}^{m}\sum_{j\in B}^{m} c_{li}c_{lj}\phi_{li}(\vec{r})\phi_{lj}(\vec{r})\end{aligned} \tag{10}$$

This integral is solved using an adaptive subspace scheme[48] to discretize the 3D grid and perform the integration.

The **intra-overlap Coulomb repulsion** $J_{\mathrm{OP}}^{\mathrm{intra}}$, within the context of the OP model, is defined as follows:

$$J_{\mathrm{OP}}^{\mathrm{intra}} = \int \rho_{\mathrm{OP}}(\vec{r_1}) r_{12}^{-1} \rho_{\mathrm{OP}}(\vec{r_2}) dr_1 dr_2 \tag{11}$$

Here, r_{12} represents the distance between points r_1 and r_2 where the overlap densities $\rho_{\mathrm{OP}}(\vec{r_1})$ and $\rho_{\mathrm{OP}}(\vec{r_2})$ are examined. Typically, ρ_{OP} is higher for electron-rich chemical bonds. In the same vein, electron-rich chemical bonds that exhibit concentrated OP density in small regions tend to have higher $J_{\mathrm{OP}}^{\mathrm{intra}}$ values.

Topological analysis of overlap density. Further insights into the shape of $\rho_{\mathrm{OP}}(\vec{r})$ can be gained through a topological analysis of the OP density, similar to the QTAIM approach. This analysis aims to identify what are referred to as overlap critical points (OCP).[18] In this context, two TOP descriptors have been recently introduced: the density in a chemical bond OCP, denoted as ρ_{OCP}, and its Laplacian, $\nabla^2\rho_{\mathrm{OCP}}$. OCPs in chemical bonds exhibit all negative curvatures, which are calculated using the Hessian of the density at the OCP, represented as:

$$\mathbf{H}_{\rho_{\mathrm{OP}}}^{\mathrm{OCP}} = \begin{bmatrix} \frac{\partial^2\rho_{\mathrm{OCP}}}{\partial x^2} & \frac{\partial^2\rho_{\mathrm{OCP}}}{\partial x\partial y} & \frac{\partial^2\rho_{\mathrm{OCP}}}{\partial x\partial z} \\ \frac{\partial^2\rho_{\mathrm{OCP}}}{\partial y\partial x} & \frac{\partial^2\rho_{\mathrm{OCP}}}{\partial y^2} & \frac{\partial^2\rho_{\mathrm{OCP}}}{\partial y\partial z} \\ \frac{\partial^2\rho_{\mathrm{OCP}}}{\partial z\partial x} & \frac{\partial^2\rho_{\mathrm{OCP}}}{\partial z\partial y} & \frac{\partial^2\rho_{\mathrm{OCP}}}{\partial z^2} \end{bmatrix} \tag{12}$$

Subsequently, $\mathbf{H}_{\rho_{\mathrm{OP}}}^{\mathrm{OCP}}$ is diagonalized to obtain the eigenvectors collected in $\mathbf{\Lambda}^{\mathrm{OCP}}$ as follows:

$$\mathbf{H}_{\rho_{\mathrm{OP}}}^{\mathrm{OCP}} = \mathbf{P}\mathbf{\Lambda}^{\mathrm{OCP}}\mathbf{P}^{-1} \tag{13}$$

In this equation, $\mathbf{P}$ is a square 3×3 matrix, with its i-th column representing the eigenvector of $\mathbf{H}_{\rho_{\mathrm{OP}}}^{\mathrm{OCP}}$, and $\mathbf{\Lambda}^{\mathrm{OCP}}$ is a diagonal matrix, with its diagonal elements as the corresponding eigenvalues, $\mathbf{\Lambda}_{ii}^{\mathrm{OCP}} = \lambda_i$. The Laplacian of the overlap density at the OCP is then defined as:

$$\nabla^2\rho_{\mathrm{OCP}} = \lambda_1 + \lambda_2 + \lambda_3 \tag{14}$$

The TOP descriptors provide insights into the shape of ρ_{OP}. Generally, a more localized overlap density ρ_{OP} leads to more negative $\nabla^2\rho_{\mathrm{OCP}}(\vec{r})$ values and larger $\rho_{\mathrm{OCP}}(\vec{r})$.[18]

Quantum theory of atoms in molecules

QTAIM bond critical point (BCP) descriptors[13] are employed here for comparison purposes. These descriptors include the total electronic density $(\rho_{r_{\mathrm{BCP}}})$ and Laplacian $(\nabla^2\rho_{r_{\mathrm{BCP}}})$ at a specific BCP, which provide insights into the charge concentration (higher $\rho_{r_{\mathrm{BCP}}}$ values and $\nabla^2\rho_{r_{\mathrm{BCP}}} < 0$) or depletion (lower $\rho_{r_{\mathrm{BCP}}}$ values and $\nabla^2\rho_{r_{\mathrm{BCP}}} > 0$) in the inter-atomic region.[13]

In addition to these descriptors, the local energy density $\mathrm{H}(r_{\mathrm{BCP}})$ at a BCP, following the Cremer-Kraka criterion,[49] is widely adopted as a measure of covalence. $\mathrm{H}(r_{\mathrm{BCP}})$ is defined as the sum of kinetic and potential energy density at the BCP: $\mathrm{H}(r_{\mathrm{BCP}})=\mathrm{G}(r_{\mathrm{BCP}}) + \mathrm{V}(r_{\mathrm{BCP}})$. The potential energy contribution is stabilizing $(\mathrm{V}(r_{\mathrm{BCP}}) < 0)$, while the kinetic energy is destabilizing $(\mathrm{G}(r_{\mathrm{BCP}}) > 0)$. Therefore, BCPs with $\mathrm{H}(r_{\mathrm{BCP}}) < 0$ are expected to exhibit a covalent character, whereas those with $\mathrm{H}(r_{\mathrm{BCP}}) > 0$ are indicative of ionic character or long-range interactions.[49] It's important to note that although exceptions have been discovered regarding the characterization of ionicity and covalency based solely on the sign of H(r_{BCP}), these findings do not diminish the significance of assessing this bond descriptor.[42,50–53] Analyzing the behavior of both $\nabla^2\rho_{r_{\mathrm{BCP}}}$ and H(r_{BCP}) has proven to be a useful approach for describing the topology of chemical bonds within the framework of QTAIM.[42]

Local Vibrational Mode Theory

Normal vibrational modes within polyatomic systems are typically delocalized.[54,55] This presents a significant challenge when one attempts to determine the intrinsic bond strength directly using normal mode frequencies and normal mode force constants. This is where the Localized Vibrational Mode (LVM) theory becomes invaluable. LVM was originally introduced by Konkoli and Cremer[56,57] and has undergone further development. For a more comprehensive understanding of LVM, including its theoretical foundation and its wide-ranging applications in chemistry and beyond, readers are encouraged to explore two recent review articles and the references therein.[9,58]

The normal vibrational modes, denoted as $\mathbf{d}_n$ and expressed in internal coordinates q_n (where $n = 1, \cdots, N_{\mathrm{vib}}$ and N_{vib} is equal to $3N-6$ for non-linear N-atomic complexes and $3N-5$ for linear N-atomic complexes), as well as the diagonal normal mode force constant matrix $\mathbf{K}$ given in normal coordinates Q_n, can be transformed into their local mode counterparts. This transformation results in local mode vectors $\mathbf{a}_n$ that are associated with internal coordinates q_n through the following expression:

$$\mathbf{a}_n = \frac{\mathbf{K}^{-1}\mathbf{d}_n^\dagger}{\mathbf{d}_n\mathbf{K}^{-1}\mathbf{d}_n^\dagger}. \tag{15}$$

The calculation of the corresponding local mode force constant k_n^a can be performed using the following expression:

$$k_n^a = \mathbf{a}_n^\dagger \mathbf{K}\mathbf{a}_n. \tag{16}$$

Local mode force constants k^a have proven to be a reliable tool for quantifying the strength of a wide range of chemical interactions.[9,58]

Computational Procedure

All geometry optimization and frequency calculations were conducted using the Domain Based Local Pair Natural Orbital Coupled Cluster (DLPNO-CCSD(T)) method,[59–61] utilizing the def2-QZVPPD basis set[62,63] and the corresponding def2-QZVPPD/C auxiliary basis.[64] Numerical gradients were applied in all calculations.

The selection of the CAS active space was based on the Natural Orbital Occupation Numbers (NOON), which are the eigenvalues obtained from the diagonalization of the first-order density matrix.[65] To determine the active space, an NBO analysis was conducted at the RI-MP2/SVP level of theory. NBOs with NOON values between 1.98 and 0.02 were adopted as active space, while the NBOs served as the initial guesses for all CAS calculations.

A wavefunction convergence test was performed for the H_2O molecule by increasing the active space from CAS(6,6) to CAS(6,30), using various basis sets including def2-TZVP, def2-TZVPPD, def2-QZVP, and def2-QZVPPD. DCD-CAS(6,6), DCD-CAS(6,8), and DCD-CAS(6,10) were also applied. These convergence tests were carried out based on the total dipole moment value and the overlap density descriptor. It should be noted that the geometry of the H_2O molecule optimized at the DLPNO-CCSD(T)/def2-QZVPPD level of theory was adopted for all CAS and DCD-CAS(2) convergence test calculations.

The X−O bond in X−OH (where X = H, Li, Na, H_2B, H_3C, H_2N, HO, F) and Li−X' (where X' = F, Cl, and Br) molecular test systems underwent analysis using CAS(10,16) (for H_2B−OH, H_3C−OH, H_2N−OH, HO−OH, and F−OH) and CAS(6,20) (for H−OH, Li−OH, Na−OH, Li−F, Li−Cl, and Li−Br). The dissociation profile of the Li–F bond was investigated using the CAS(2,6) method, along with its correction at the DCD-CAS(2) level of theory. The calculation of OP/TOP descriptors utilized CAS and DCD-CAS(2) (For Li–F) wavefunctions, whereas QTAIM counterparts were determined through CAS calculations for the molecules in equilibrion geometries. Since the equilibrium geometries of the test systems were determined using the DLPNO-CCSD(T)/def2-QZVPPD level of theory, the LVM analysis was also performed at the same level.

All geometry optimization, frequency calculations, CAS, and DCD-CAS(2) single-point calculations were conducted using Orca 5.0.[66] OP/TOP descriptors were obtained using our ChemBOS software, available at www.chembos.website,[16,48] while QTAIM descriptors were computed using Molden2aim[67] and MultiWFN[68] software. LVM analyses were performed using the LModeA package.[69] Details regarding the Orca(*output*) → (*input*)ChemBOS conversion tools can be found in Figure S20 in Support Information.

Results and Discussion

The introduction of OP/TOP descriptors relied on the computation of Localized Molecular Orbitals (LMOs). However, localization techniques depend on atomic charge based methods and may involve various charge partitions, which can influence the LMOs and, consequently, the OP/TOP descriptors. On the other hand, applying Equation 9 necessitates an MCSCF procedure in which both the coefficients c_{li} of the molecular orbitals (MOs) and the coefficients $\mathbb{C}_k$ of the configuration state functions (CSFs) are optimized. This implies the need to use canonical MOs instead of localized MOs due to the potential loss of the locality of LMOs after an MCSCF calculation. Therefore, demonstrating that the overlap density can be obtained from a canonical MO basis is crucial for extending OP/TOP descriptors from an MCSCF wavefunction. To address this, Figure 2 illustrates the equivalence between the overlap density obtained through a single-determinant (HF) wave function (Equation 4), using localized MOs (Figure 2a), and canonical MOs (Figure 2b).

It is noticeable that both ρ_{OP} and $J_{\mathrm{OP}}^{\mathrm{intra}}$ are higher when localized MOs are employed. Additionally, ρ_{OCP} exhibits similar behavior. On the other hand, $\nabla^2\rho_{\mathrm{OCP}}(\vec{r})$ assumes more negative values. This indicates a slightly higher charge concentration in the overlap density when localized MOs are utilized, possibly as a result of LMOs being designed to maximize electron density locality. Interestingly, it is observed that the localized nature of the overlap density is preserved even when canonical MOs are adopted. This equivalence leads to highly similar OP/TOP descriptors, allowing for the use of canonical MOs as a suitable basis for obtaining the overlap density and its OP/TOP descriptors.

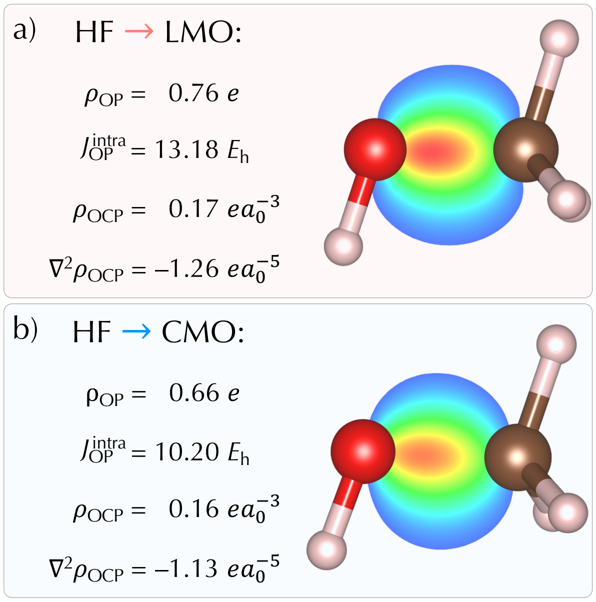

Figure 2: OP/TOP descriptors for the C–O bond in $H_3C{-}OH$ obtained using localized MOs (a) and canonical MOs (b). $\rho_{\mathrm{OP}}(\vec{r})$ maps ranging from 0 to 0.16 e/a_0^3 in a red-green-blue color scheme. Calculations at the HF/def2-TZVP level of theory.

Active Space size convergence

As a consequence of the variational theorem, the closer the CASSCF energy is to the exact energy, the more the approximate wavefunction approaches the exact one. The convergence of CASSCF wavefunctions has been a subject of study for some time, and it's well-known that properties other than energy converge with the active space size in a different manner than energy. Moreover, it has been established[70] that certain properties, such as molecular dipole and polarizability, exhibit weak dependence on the size of the active space. This behavior can be seen as an indication of convergence with respect to the active space size or as a sign of very slow convergence of the dynamic correlation contribution to the properties under study. It's important to note that even with a large active space in CASSCF, it may not fully account for a significant portion of dynamic correlation. However, in cases where this type of correlation is not dominant, demonstrating CASSCF convergence with the active space size remains crucial.

Figure 3 shows the molecular dipole moment (Figure 3a) and overlap density integral ρ_{OP} (Figure 3b) for different active spaces sizes and different basis sets.

It is observed that the inclusion of extra polarization and diffuse function at basis sets def2-TZVPPD and def2-QZVPPD lead to equivalent values of both dipole (CAS(6,22) and higher) and ρ_{OP} (CAS(6,16) and higher). Interstingly, from CAS(6,16) to CAS(6,22), even with different molecular dipole moments, the overlap density integral for O–H bonds assume the same values for both def2-TZVPPD and def2-QZVPPD basis.

The dipole moment is observed to be weakly dependent on basis set and for active space size for CASSCF(6,22) and higher. It is worthy noting that the CASSCF(6,22–30) value for H_2O dipole moment reported here is close to 1.846 Debye, in line with the reference CCSD=FULL/daug-cc-pVTZ value of 1.864 Debye from the NIST Computational Chemistry Comparision and Benchmark Database.[71]

These results, despite being obtained for the small H_2O molecule, clearly demonstrate that when we treat the wavefunction as exact (or in practice, a converged wavefunction for the chosen finite basis set), all properties, including overlap density descriptors, can be computed accurately. Moreover, since the converged wavefunction is not influenced by increases in the finite basis set or the inclusion of CASSCF, we can conclude that overlap descriptors are also not dependent on these factors.

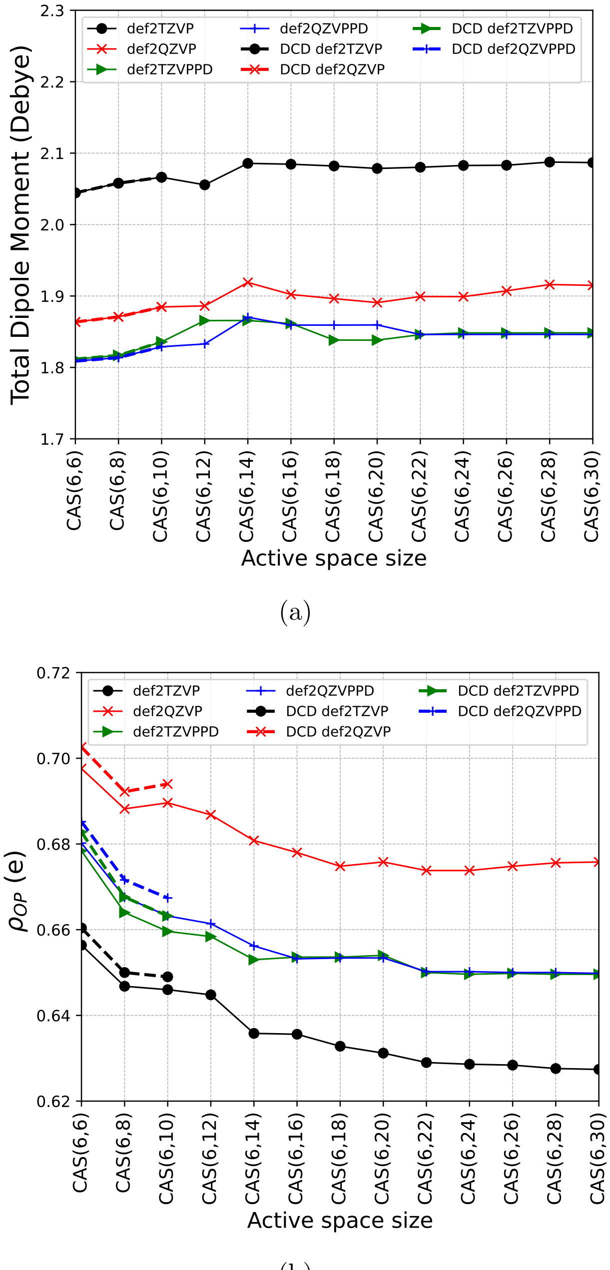

(a)

(b)

Figure 3: Variations in molecular dipole moment (a) and O–H overlap density ρ_{OP} (b) with active space size in H_2O for different basis sets. The calculations were conducted using CASSCF active space sizes ranging from 6 to 30 and the DCD-CAS active space sizes from 6 to 10.

QTAIM and LVM trends in test systems

The chosen test systems accurately represent various changes in the bonding situations arising from different chemical environments. Molecules numbered from **1** to **8** in Figure 1 encompass X–OH bonds with a diverse range of interaction classifications, encompassing polar covalent, charge-shift bonds, and ionic bond types. Fugel and collaborators[42] conducted a comprehensive analysis primarily using DFT methodologies. Their bond analysis encompasses a wide range of bond descriptors, although it does not include OP/TOP and LVM descriptors. Additionally, it's worth noting that our test systems **1**, and **9-11** were not considered in Fugel's report.

Table 1 provides a comprehensive summary of the obtained results for each chemical bond descriptor across all test systems. Notably, all QTAIM results are consistent with those previously reported by Fugel and collaborators.[42]

In general, for test systems ranging from **1** to **3**, it is observed that the H–O bond is the sole covalent bond, exhibiting both H_{BCP} and $\nabla^2\rho_{OCP}$ with negative values. These negative values indicate a shared interaction ($H_{BCP} < 0$) and a bond charge concentration ($\nabla^2\rho_{OCP} < 0$). In test systems **2** and **3**, the bond distance gradually increases, followed by a slight decrease in the already low values of $\rho_{r_{BCP}}$. From Li–OH to Na–OH bonds, there are low positive values for H_{BCP} and relatively high positive values for $\nabla^2\rho_{OCP}$, that decrease from Li to Na. This suggests that these bonds are primarily determined by electrostatic interactions and are characterized as ionic in nature. The local force constants of X–OH in test systems **1-3** qualitatively agree with bond distance, with k_a values decreasing as the bond distance increases, following the order k_a(H–OH) > k_a(Li–OH) > k_a(Na–OH).

Test systems **4-8** demonstrate variations in the bond situations for X–OH with X ranging from B to F. The results are generally consistent with those reported by Fugel and collaborators,[42] with some slight differences, likely attributable to the different computational methods (single- vs. multi-determinant) employed. As expected, B–O exhibits a positive $\nabla^2\rho_{OCP}$ and a negative H_{BCP}, characterizing it as a highly polarized covalent bond. In contrast, C–O and N–O are classified as polarized covalent bonds due to both $\nabla^2\rho_{OCP}$ and H_{BCP} being negative. The O–O bond shows a negative H_{BCP} and a positive, nearly zero $\nabla^2\rho_{OCP}$, which increases in the case of the F–O bond.

It's worth noting that both O–O (in HOOH) and F–O (in FOH) bonds are characterized as being stabilized by the resonance of ionic forms rather than the covalent sharing of electrons, known as charge-shift bonds (CSBs).[72] A characteristic of CSBs is that the electron density between the bonded atoms is predicted to be low, which is not entirely reflected in the high values of $\rho_{r_{BCP}}$ for O–O and F–O bonds obtained from QTAIM.

From the perspective of LVM theory, the local force constants decrease in the series from B to F, with the exception of the HO–OH case, which exhibits an increased k_a value. In this sense, the O–O bond is stronger than the C–O and N–O bonds in test systems **5** and **6**.

Test systems **9–11** (Li–F, Li–Cl, and Li–Br) exhibit small and positive ρ_{BCP} and HBCP, both decreasing along the series. Additionally, the high and positive $\nabla^2\rho r_{BCP}$ value also decreases along this series. These values indicate charge depletion in these bonds ($\nabla^2\rho_{r_{BCP}} > 0$) and major electrostatic interactions ($H_{BCP} > 0$). The local force constants for test systems **9–11** agree with the normal mode force constants, but their behavior does not follow either the bond distances or the QTAIM descriptors.

OP/TOP descriptors for studied molecules

Firstly, it's important to consider the performance and computational demands of CASSCF calculations in the context of OP/TOP descriptors. CASSCF calculations are well-known for their time-consuming nature, and the computational resources required increase significantly with the size of the basis set and the active space.[73] For the sake of comparison, a CAS(6,6) calculation generates a total of 141

Table 1: Results for test examples **1-11** (see Figure 1): bond distance r (in Å), overlap density ρ_{OP} (in e), intra-overlap repulsion $J_{\mathrm{OP}}^{\mathrm{intra}}$ (in E_{h}), overlap critical point density ρ_{OCP} (in e/a_0^3), Laplacian of ρ_{OCP} at OCP $\nabla^2\rho_{\mathrm{OCP}}$ (in e/a_0^5), electron density at BCP $\rho_{r_{\mathrm{BCP}}}$ (in e/a_0^3), local energy density $\mathrm{H}_{\mathrm{BCP}}$ (in E_{h}/a_0^3), Laplacian of $\rho_{r_{\mathrm{BCP}}}$ (in e/a_0^5), and local bond stretching force constant k_a (in mDyn/Å)

#	Bond	r	ρ_{OP}	$J_{\mathrm{OP}}^{\mathrm{intra}}$	ρ_{OCP}	$\nabla^2\rho_{\mathrm{OCP}}$	$\rho_{r_{\mathrm{BCP}}}$	$\mathrm{H}_{\mathrm{BCP}}$	$\nabla^2\rho_{r_{\mathrm{BCP}}}$	k_a
1	H−OH	0.96	0.654	9.926	0.188	-1.796	0.370	-0.810	-2.860	8.400
2	Li−OH	1.59	0.878	11.526	0.108	-1.262	0.072	0.014	0.667	2.604
3	Na−OH	1.94	0.229	0.649	0.017	-0.174	0.051	0.011	0.430	1.877
4	H_2B−OH	1.35	0.749	12.000	0.165	-1.531	0.215	-0.195	1.029	6.479
5	H_3C−OH	1.42	0.577	7.749	0.137	-1.064	0.265	-0.426	-0.692	4.689
6	H_2N−OH	1.44	0.369	3.837	0.116	-0.865	0.294	-0.268	-0.372	4.294
7	HO−OH	1.45	0.280	2.369	0.101	-0.777	0.283	-0.204	0.020	5.595
8	F−OH	1.43	0.244	1.856	0.098	-0.899	0.280	-0.190	0.230	4.096
9	Li−F	1.57	0.554	6.391	0.166	-3.440	0.077	0.014	0.718	3.891
10	Li−Cl	2.03	0.644	5.934	0.045	-0.216	0.044	0.005	0.276	1.401
11	Li−Br	2.18	0.657	5.641	0.033	-0.125	0.038	0.003	0.208	2.103

CSFs, whereas a CAS(6,30) calculation generates an impressive number of approximately 1.4×10^6 CSFs. This significant increase in the number of CSFs highlights the computational challenge when using larger active spaces (see Figure S1 in Support Information). However, once the CASSCF calculation has converged, the number of configuration state functions (CSFs) needed to generate both the total electron density and the overlap density depends on the specific system. Generally, fewer than 50 CSFs are required for an accurate wavefunction description. Our implementation in ChemBOS efficiently handles CSFs determinants and demonstrates good parallel performance. To provide a reference, when running a CASSCF(6,6)/def2-QZVPPD calculation for the test system H_2O, ChemBOS achieves an impressive speedup of approximately 105 when executed with 128 threads on an AMD EPYC 7763 with 512 GB of RAM (details can be found in Figure S16 in the Support Information).

The increase in bond polarization, as captured by QTAIM through $\nabla^2\rho_{r_{\mathrm{BCP}}}$ and $\mathrm{H}_{\mathrm{BCP}}$ descriptors, is interpreted as a decrease in covalent character. This aligns with the well-established Bent's rule,[74] which posits that bonds between elements of varying electronegativities tend to be polar, causing the electron density in such bonds to shift towards the more electronegative element. Recently, Alabugin and colleagues[75] used a polarization percentage (Pol%) calculated as the square of natural hybrid orbital (NHO) coefficients in the bonding NBOs from MP2/6-311++G(d,p) level of theory and reported results consistent with Bent's rule, showing that polarization towards X (in H_nX–OH) bonds increases from B–O to F–O.

In a similar vein, other chemical bond descriptors are anticipated to yield chemically meaningful values that align with these trends. According to the OP model, chemical bonds formed between atoms with different electronegativities are likely to exhibit overlap density ($\rho_{\mathrm{OP}}(\vec{r})$) shifted towards the more electronegative atom. Profiles of $\rho_{\mathrm{OP}}(\vec{r})$ along the bond axis for test systems **1-11** are presented in Figure 4.

It is evident that $\rho_{\mathrm{OP}}(\vec{r})$ tends to be more concentrated around the most electronegative atom and less dispersed in the bonding region, consistent with the expected behavior. ρ_{OP} represents the two-center contribution of a specific bond to the total electron density and generally has higher values for electron-rich chemical bonds. This trend is also evident in Table 1 and Figure 4. Across all subgroups (test systems **1**–**3**, **4**–**8**, and **9**–**11**), the overlap critical point density (ρ_{OCP}) decreases as one transitions from H to Na in O–X bonds for test systems **1**–**3**, from B to F in test systems **4**–**8**, and from F to Br in Li–X bonds for test systems **9**–**11**.

In the series of alkali (and hydrogen) hydroxides (test systems **1**–**3**), the H–O bond stands out with the highest ρ_{OCP} and $\nabla^2\rho_{\mathrm{OCP}}$ values, even though it doesn't have the highest ρ_{OP} and $J_{\mathrm{OP}}^{\mathrm{intra}}$ values when compared to the Li–OH bond. This distinction arises from the inherently polar covalent nature of the H–O bond, as revealed by the QTAIM analysis. Additionally, hydrogen (H) lacks core electron shells, which further contributes to these differences. Consequently, the overlap density in H–O bond is distributed throughout the entire bond region but predominantly concentrates along the bond axis (as depicted in the gray plot in Figure 4a). As we progress down the Periodic Table, moving from Li to Na, a significant decrease in overlap density becomes evident, primarily due to the heightened ionic character of these bonds. 2D color maps of the overlap density for test systems **1**–**3** are available in the Support Information.

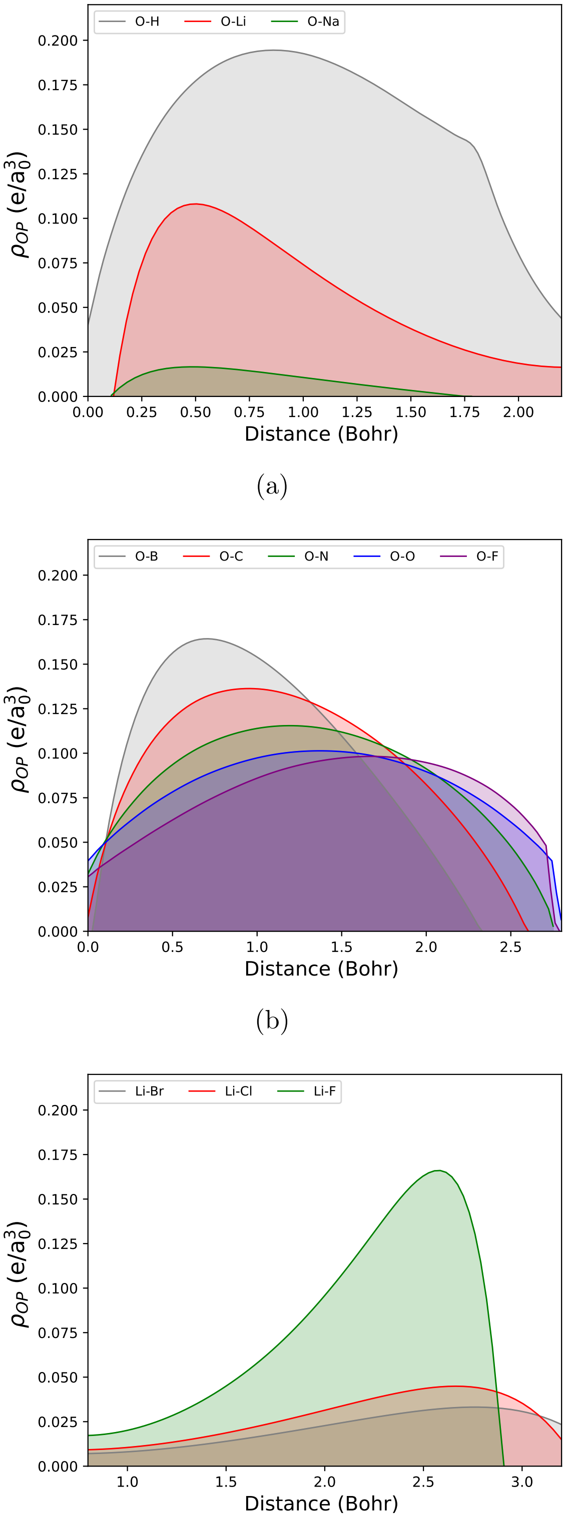

(a)

(b)

(c)

Figure 4: Profiles of $\rho_{\mathrm{OP}}(\vec{r})$ along the bond axis for test systems **1-11**. In plots (a) and (b), the oxygen atoms are depicted on the left side, while in plot (c), it is the lithium atom. Calculations were performed at the CASSCF/def2-QZVPPD level of theory (details in Computational Procedure section).

In test systems **4**–**8**, the B–O bond, which has the highest ρ_{OCP} in the series and is less spread (exhibiting the most negative $\nabla^2\rho_{\mathrm{OCP}}$), also exhibits the largest $J_{\mathrm{OP}}^{\mathrm{intra}}$. The qualitative scenario of overlap charge spreading across the chemical bond is quantified by the ρ_{OCP} and $\nabla^2\rho_{\mathrm{OCP}}$ descriptors, indicating less spread (i.e., less negative $\nabla^2\rho_{OCP}$) bonds from C–O to F–O, as illustrated in Figure 4b and Figure 5.

Figure 5 is equipped with lines that pass through the middle of the bonds, aiding the visualization of bond overlap density polarization toward the more electronegative atom. An observable trend is the gradual decrease in the values of ρ_{OP}, ρ_{OCP}, and $J_{\mathrm{OP}}^{\mathrm{intra}}$ as we progress from B–O to F–O. Notably, $\nabla^2\rho_{\mathrm{OCP}}$ becomes less negative up to O–O, but then increases for the F–O bond. Local bond stretching (k*a*) inversely follows the trend of $\nabla^2\rho_{\mathrm{OCP}}$, decreasing along the series but inverting the behavior for HO–OH. It's interesting to note that QTAIM does not align with the trends observed in both OP/TOP and LVM analyses.

It's interesting to note that QTAIM indicates that the B–O bond is associated with a relatively high negative value of $\mathrm{H_{BCP}}$, which Fugel[42] attributed to the additional orbital overlap arising from the B–O π bond. The ρ_{OP}

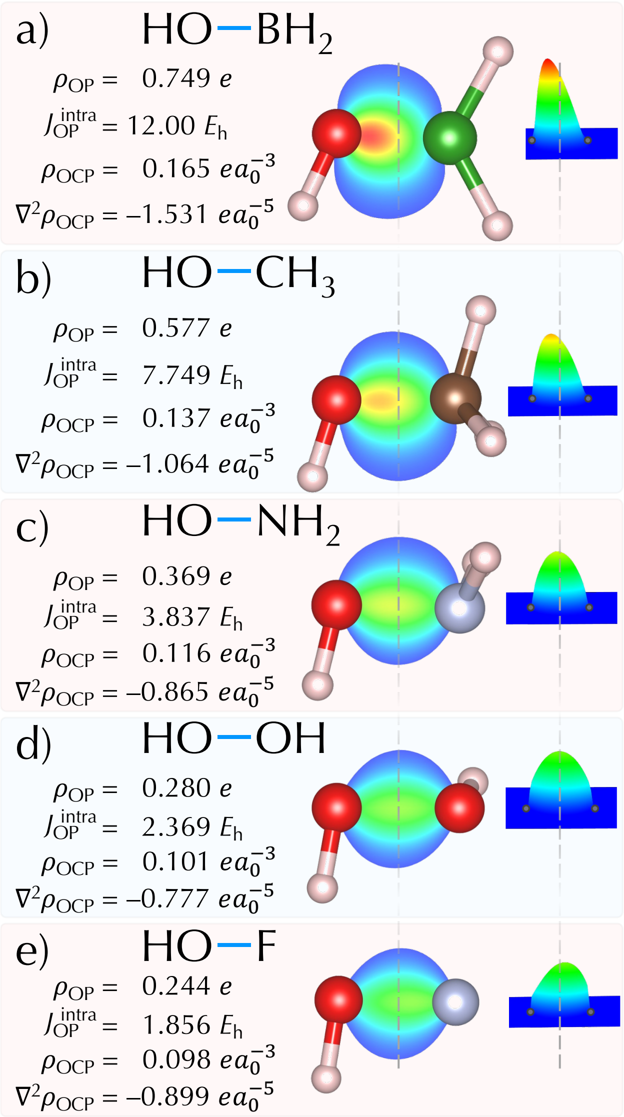

Figure 5: OP/TOP descriptors and $\rho_{\text{OP}}(\vec{r})$ maps for O–X bonds, where X = BH_2, CH_3, NH_2, OH, and F. The vertical lines indicate the midpoint of the bonds in the $\rho_{\text{OP}}(\vec{r})$ maps, ranging from 0 to 0.16 e/a_0^3 in a red-green-blue color scheme. Calculations were performed at the CASSCF/def2-QZVPPD level of theory.

values in Table 1 take into account the overlaps between all MOs of different shapes in a multiconfigurational fashion, and indeed, the B–O bond exhibits a high ρ_{OP} value, which can be attributed to the extra stabilization of this bond. This extra stabilization is also supported by LVM analysis, which identifies the B–O bond as the strongest in the series of test systems from B–O to F–O.

In test systems **9**–**11**, which include Li–F, Li–Cl, and Li–Br bonds, we observe the same trend as in the other test system groups, where ρ_{OP} increases with increasing covalency or decreasing ionicity. However, there is an interesting difference between these two groups of systems. In test systems **1**–**8**, higher values of ρ_{OP} are generally followed by high values of $J_{\text{OP}}^{\text{intra}}$. In test systems **9**–**11**, on the other hand, we notice that as ρ_{OP} increases, $J_{\text{OP}}^{\text{intra}}$ decreases.

A more detailed analysis of TOP descriptors reveals that in the Li–X series, where X ranges from F to Br, the variation in $\nabla^2\rho_{\text{OCP}}$ is much more pronounced. For example, it is -3.440 e/a_0^5 for Li–F and -0.125 e/a_0^5 for Li–Br. Essentially, as we move from Li–F to Li–Br, the overlap density becomes significantly more spread along the bond region, as measured by $\nabla^2\rho_{\text{OCP}}$ (as seen in Figure 4c). This leads to a drop in $J_{\text{OP}}^{\text{intra}}$ even though there is an increase in the overlap density integral.

OP/TOP descriptors Li–F bond dissociation

We selected the dissociation pattern of the Li–F bond to highlight the differences in OP/TOP descriptors when utilizing CASSCF and a second-order corrected wavefunction, specifically the Orca implementation DCD-CAS(2). In this example, we utilized a state-averaged CAS(2,6) wavefunction, giving equal weights to the ground and first excited states. This active space includes the molecular orbital mainly composed of a p_z orbital located on the F atom, with small contributions from Li s-type atomic orbitals (illustrated in Figure 6a and referred to as MO-A), and a σ-type orbital primarily composed of Li s-type orbitals with small contributions from F s- and p_z-type atomic orbitals (depicted in Figure 6b and referred to as MO-B), among others.

At the equilibrium geometry, which is close to 1.5 Å, the ground state is primarily characterized by the CSF involving MO-A, with a doubly occupied status. The CSF composed of MO-B at a Li–F distance of 1.5 Å has negligible weight. However, as the dissociation of the Li–F molecule proceeds, both the weights (CASSCF coefficients) and MO shapes undergo significant changes.

MO-A gradually loses its Li s-type character, while the weight of the CSF involving both MO-A and MO-B as single occupied orbitals increases. As depicted in Figure 6, at approximately 4.1 Å, an inversion in weights occurs, with the CSF where both MO-A and MO-B are singly occupied having the larger coefficient. At greater distances (6.5 Å in Figure 6), MO-A is characterized by a pure $2p_z$ orbital at the F atom, while MO-B exhibits a pure 2s orbital at the Li atom. At this point, it can be considered that two neutral species are formed, with each MO having one electron.

It's important to mention that CASSCF calculations usually predict an avoided crossing point (between ground and excited states energies) at a distance of approximately 4.1 Å, as reported in previous studies.[41,76] In contrast, a Full CI reference indicates an avoided crossing occurring at roughly 6.6 Å,[77] and DCD-CAS(2) calculations with a CAS(2,2) active space result in a crossing point at 5.65 Å.[41]

While the CASSCF (or other more accurate) wavefunction coefficients provide valuable insights into the ionic/neutral nature of the chemical species, it is equally important to evaluate how chemical bond descriptors capture the changes in the wavefunction as a bond is broken. In this context, Figure 7 presents OP/TOP descriptors along the dissociation profile of the Li–F ground state using the CAS(2,6) wavefunction, as well as its correction at the DCD-CAS(2) level of theory. These curves focus on the range of 3.0 to 6.5 Å, covering the crossing points for both CASSCF and DCD-CAS(2) wavefunctions. Generally, for a given distance, the DCD-CAS(2) wavefunction yields higher values of ρ_{OP}, ρ_{OCP}, and $J_{\mathrm{OP}}^{\mathrm{intra}}$

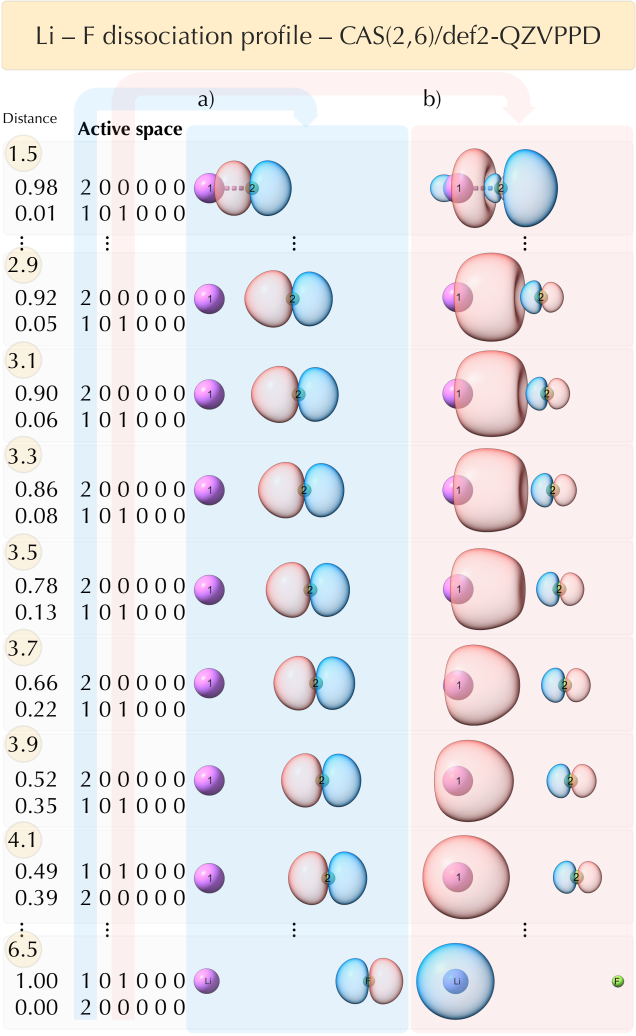

Figure 6: Visualization of the two primary molecular orbitals (MOs) constituting the CAS(2,6) wavefunction during the Li–F dissociation process. Label 1 refers to Li and 2 to F atom. MO (a) is predominantly composed of F p_z-type atomic orbitals, while MO (b) is mainly derived from Li s-type atomic orbitals. Each box corresponds to a specific distance along the Li–F dissociation, displaying CASSCF coefficients and information about the compositions CSFs. The numbers within each CSF denote the occupation of the respective MO, with blue representing (a) and red representing (b). MOs are depicted with isosurfaces set at 0.05 e/a_0^3

compared to the CASSCF counterpart. Additionally, $\nabla^2\rho_{\mathrm{OCP}}$ is more negative with the DCD-CAS(2) wavefunction.

It is worth noting that OP/TOP descriptors sensitively reflect the ionic/neutral inversion in each type of wavefunction along the Li–F dissociation profile. Figure 7c shows that ρ_{OCP} drops to nearly zero precisely at the Li–F distance of 4.1 Å, the point at which the CSFs inversion occurs. $J^{\mathrm{intra}}_{\mathrm{OP}}$ and $\nabla^2\rho_{\mathrm{OCP}}$ approach zero for distances above 4.1 Å. The overlap density integral exhibits an interesting behavior. It experiences a significant decrease near 4.1 Å, but then ρ_{OP} gradually decreases, becoming similar to the DCD-CAS(2) counterpart at a Li–F distance of 5.5 Å. This indicates that even when the neutral determinant dominates (with neutral Li having one electron in the 2s orbital and neutral F with a hole in the 2pz orbital), there is still some orbital overlapping occurring.

Both CASSCF and DCD-CAS(2) yield ρ_{OP} values that approach zero at approximately 6.5 Å. Specifically, for the CAS(2,6) wavefunction, ρ_{OP} vanishes close to 4.1 Å, whereas for the DCD-CAS(2) counterpart, this occurs near 6.1 Å. The disparity in the zero points of ρ_{OP} and ρ_{OCP} suggests a widely distributed overlap density, with its maximum critical point close to zero but still maintaining integrated overlap density. These insightful details about the MCSCF wavefunction, as provided by OP/TOP, can pave the way for novel applications in understanding chemical bond dynamics across various multiconfigurational and multireference classes of wavefunctions.

Conclusions

In conclusion, this study delved into the realm of chemical bond descriptors, focusing on the extension of OP/TOP descriptors using MCSCF wavefunctions. Through a comparative analysis of CASSCF wavefunctions for various molecular systems, including the X−O and Li−X' test systems, we gained valuable insights into the behavior of these descriptors. The equivalence demonstrated between canonical and localized molecular orbitals offers a

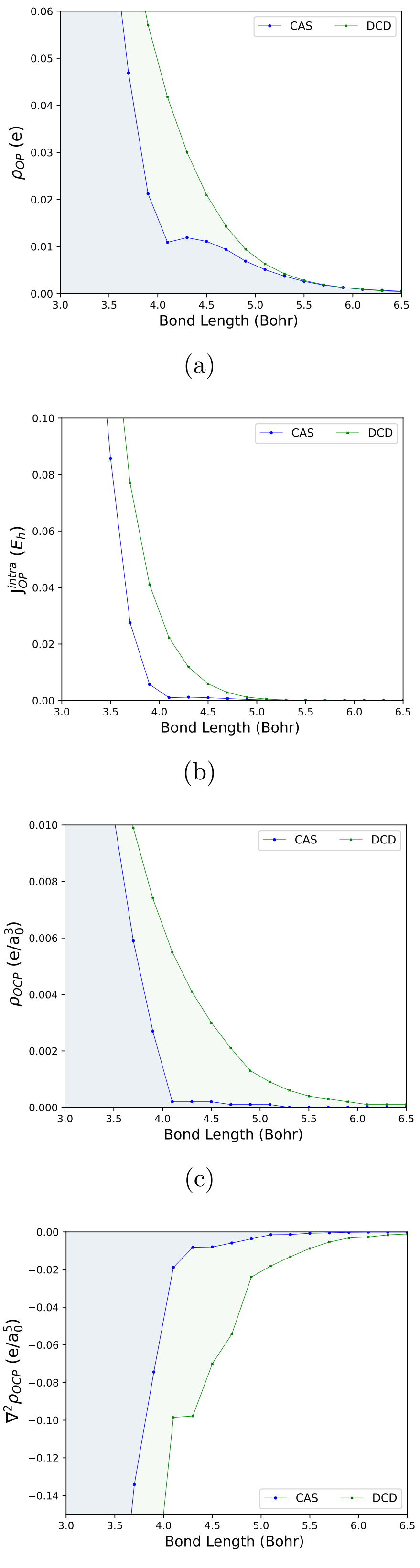

(a)

(b)

(c)

(d)

Figure 7: OP/TOP descriptors: (a) ρ_{OP}, (b) J^{intra}_{OP}, (c) ρ_{OCP}, and (d) $\nabla^2\rho_{OCP}$ (d) for Li–F bond dissociation profile using CASSCF(2,6) and DCD-CASSCF(2,6) wavefunctions.

practical approach to compute overlap densities and OP/TOP descriptors accurately. Furthermore, the results highlighted the importance of converged wavefunctions in achieving precise property calculations.

Our investigation encompassed a broad spectrum of molecular systems, including X−O bonds in X−OH and Li−X' interactions, each subjected to CAS(10,16) and CAS(6,20) calculations. These analyses challenged the MCSCF-based OP/TOP bond descriptors, offering valuable insights and allowing for comparisons with QTAIM and LVM descriptors.

While QTAIM and LVM descriptors aligned with existing literature, they fell short in explaining certain trends observed in our study. In contrast, OP/TOP descriptors, guided by the OP model, demonstrated that chemical bonds formed between atoms with differing electronegativities tend to exhibit overlap density shifted towards the more electronegative atom. This effect was quantified using ρ_{OCP} and $\nabla^2\rho_{\mathrm{OCP}}$ descriptors, which indicated reduced spreading (i.e., less negative $\nabla^2\rho_{OCP}$) in bonds with increasing electronegativity differences.

Additionally, our analysis of the Li–F dissociation profile revealed that OP/TOP descriptors sensitively reflected the ionic/neutral inversion along the Li–F dissociation pathway. The overlap density integral exhibited a distinctive behavior, experiencing a significant decrease near 4.1 Å, followed by a gradual decrease in ρ_{OP}, aligning with the DCD-CAS(2) counterpart at a Li–F distance of 5.5 Å. The analysis of ρ_{OCP} and $\nabla^2\rho_{\mathrm{OCP}}$ along the dissociation pathway suggests a widely distributed overlap density near the ionic/neutral inversion. This intriguing observation suggests that even when the neutral determinant dominates, with neutral Li possessing one electron in the 2s orbital and neutral F exhibiting a hole in the 2pz orbital, some degree of orbital overlap persists.

Notably, OP/TOP descriptors provided unique perspectives on chemical bond dynamics, particularly in the context of multiconfigurational and multireference wavefunctions. The sensitivity of OP/TOP descriptors to ionic/neutral inversion during Li–F dissociation showcased their potential in elucidating intricate bond phenomena. These findings open the door to novel applications in understanding chemical bond dynamics across diverse wavefunction classes, further advancing our comprehension of molecular properties and chemical interactions.

Acknowledgement The authors are grateful for the financial support from CNPq and CAPES agencies. The authors thank SMU and NPAD/UFRN for generously providing computational resources. This work was funded by the Brazilian Public Call n. 03 Produtividade em Pesquisa PROPESQ/PRPG/UFPB project number PVN13305-2020 and CAPES Demanda Social 88887.659768/2021-00.

Supporting Information Available

The following file is available free of charge.

- ACS-OP-TOP-SuppInfo.pdf

Supplementary data associated with this article can be found online. This includes tables with the QTAIM and OP/TOP results for single and double bonds, overlap density maps, and Cartesian coordinates of test systems.

References

(1) Lewis, G. N. THE ATOM AND THE MOLECULE. *J. Am. Chem. Soc.* **1916**, *38*, 762–785.

(2) Feynman, R. P. Forces in Molecules. *Phys. Rev.* **1939**, *56*, 340–343.

(3) Coulson, C. A. The contributions of wave mechanics to chemistry. *J. Chem. Soc.* **1955**, 2069–2084.

(4) Pauling, L. The nature of the chemical bond—1992. *J. Chem. Educ.* **1992**, *69*, 519.

(5) Kitaura, K.; Morokuma, K. A new energy decomposition scheme for molecular interactions within the Hartree-Fock approximation. *Int. J. Quantum Chem.* **1976**, *10*, 325–340.

(6) Mo, Y.; Gao, J.; Peyerimhoff, S. D. Energy decomposition analysis of intermolecular interactions using a block-localized wave function approach. *J. Chem. Phys.* **2000**, *112*, 5530–5538.

(7) Levine, D. S.; Head-Gordon, M. Energy decomposition analysis of single bonds within Kohn-Sham density functional theory. *PNAS* **2017**, *114*, 12649–12656.

(8) Bickelhaupt, F. M.; Houk, K. N. Analyzing Reaction Rates with the Distortion/Interaction-Activation Strain Model. *Angew. Chem. Int. Ed.* **2017**, *56*, 10070–10086.

(9) Kraka, E.; Quintano, M.; Force, H. W. L.; Antonio, J. J.; Freindorf, M. The Local Vibrational Mode Theory and Its Place in the Vibrational Spectroscopy Arena. *J. Phys. Chem. A* **2022**, *126*, 8781–8900.

(10) Moura Jr., R. T.; Quintano, M.; Santos-Jr, C. V.; Albuquerque, V. A.; Aguiar, E. C.; Kraka, E.; Carneiro Neto, A. N. Featuring a new computational protocol for the estimation of intensity and overall quantum yield in lanthanide chelates with applications to Eu(III) mercapto-triazole Schiff base ligands. *Opt. Mater.: X.* **2022**, *16*, 100216–1–100216–15.

(11) Moura, Jr., R. T.; Quintano, M.; Antonio, J. J.; Freindorf, M.; Kraka, E. Automatic Generation of Local Vibrational Mode Parameters: From Small to Large Molecules and QM/MM Systems. *J. Phys. Chem. A* **2022**, *126*, 9313–9331.

(12) Quintano, M.; Moura Jr., R. T.; Kraka, E. The pK_a rule in light of local mode force constants. *Chem. Phys. Lett.* **2023**, *826*, 140654–1–140654–7.

(13) Bader, R. F. W. A quantum theory of molecular structure and its applications. *Chem. Rev.* **1991**, *91*, 893–928.

(14) Savin, A.; Nesper, R.; Wengert, S.; Fässler, T. F. ELF: The Electron Localization Function. *Angew. Chem.* **1997**, *36*, 1808–1832.

(15) Weinhold, F.; Landis, C.; Glendening, E. What is NBO analysis and how is it useful? *Int. Rev. Phys. Chem.* **2016**, *35*, 399–440.

(16) Moura Jr., R. T.; Neto, A. N. C.; Malta, O. L.; Longo, R. L. Overlap properties of chemical bonds in generic systems including unusual bonding situations. *J. Mol. Model* **2020**, *26*.

(17) Malta, O.; Batista, H.; Carlos, L. Overlap polarizability of a chemical bond: a scale of covalency and application to lanthanide compounds. *Chem. Phys.* **2002**, *282*, 21–30.

(18) Santos, C. V.; Monteiro, S. A.; Soares, A. S. C.; Souto, I. C. A.; Moura Jr., R. T. Decoding Chemical Bonds: Assessment of the Basis Set Effect on Overlap Electron Density Descriptors and Topological Properties in Comparison to QTAIM. *J. Phys. Chem. A* **2023**, *127*, 7997–8014.

(19) Carlos, L.; Malta, O.; Albuquerque, R. A covalent fraction model for lanthanide compounds. *Chem. Phys. Lett.* **2005**, *415*, 238–242.

(20) Malta, O. L.; Moura Jr., R. T.; Longo, R. L. Electron energy-loss cross sections for the chemical bond overlap plasmon Of the hydrogen molecule. *J. Braz. Chem. Soc.* **2010**, *21*, 476–480.

(21) Moura Jr., R. T.; Duarte, G. C. S.; da Silva, T. E.; Malta, O. L.; Longo, R. L. Features of chemical bonds based on the overlap polarizabilities: diatomic and solid-state systems with the frozen-density embedding approach. *Phys. Chem. Chem. Phys.* **2015**, *17*, 7731–7742.

(22) Santos-Jr, C. V.; de Souza, M. A. F.; Kraka, E.; Moura Jr., R. T. Analysis of spectator chemical bonds in SN2@C and @Si reaction mechanisms in the gas phase. *Chem. Phys. Lett.* **2022**, *787*, 139282.

(23) Moura Jr., R. T.; Neto, A. N. C.; Longo, R. L.; Malta, O. L. On the calculation and interpretation of covalency in the intensity parameters of 4f—4f transitions in Eu^{3+} complexes based on the chemical bond overlap polarizability. *J. Lumin.* **2016**, *170*, 420–430.

(24) Neto, A. N. C.; Moura Jr., R. T.; Aguiar, E. C.; Santos, C. V.; de Medeiros, M. A. Theoretical study of geometric and spectroscopic properties of Eu(III) complexes with Ruhemann's Purple ligands. *J. Lumin.* **2018**, *201*, 451–459.

(25) Carneiro Neto, A. N.; Moura Jr., R. T. Overlap integrals and excitation energies calculations in trivalent lanthanides 4f orbitals in pairs Ln-L (L = Ln, N, O, F, P, S, Cl, Se, Br, and I). *Chem. Phys. Lett.* **2020**, *757*, 137884.

(26) Moura Jr., R. T.; Malta, O. L.; Longo, R. L. The chemical bond overlap plasmon as a tool for quantifying covalency in solid state materials and its applications to spectroscopy. *Int. J. Quantum Chem.* **2011**, *111*, 1626–1638.

(27) Moura Jr., R. T.; Oliveira, J. A.; Santos, I. A.; de Lima, E. M.; Carlos, L. D.; Aguiar, E. C.; Neto, A. N. C. Theoretical Evidence of the Singlet Predominance in the Intramolecular Energy Transfer in Ruhemann's Purple Tb(III) Complexes. *Adv. Theory Simul.* **2021**, *4*, 2000304.

(28) Moura Jr., R. T.; Neto, A. N. C.; Aguiar, E. C.; Santos-Jr., C. V.; de Lima, E. M.; Faustino, W. M.; Teotonio, E. E.; Brito, H. F.;

Felinto, M. C.; Ferreira, R. A.; Carlos, L. D.; Longo, R. L.; Malta, O. L. (INVITED) JOYSpectra: A web platform for luminescence of lanthanides. *Opt. Mater.: X* **2021**, *11*, 100080.

(29) Moura Jr., R. T.; Quintano, M.; Santos-Jr, C. V.; Albuquerque, V. A.; Aguiar, E. C.; Kraka, E.; Carneiro Neto, A. N. Featuring a new computational protocol for the estimation of intensity and overall quantum yield in lanthanide chelates with applications to Eu(III) mercapto-triazole Schiff base ligands. *Opt. Mater.: X* **2022**, *16*, 100216.

(30) Becke, A. D. Perspective: Fifty years of density-functional theory in chemical physics. *J. Chem. Phys.* **2014**, *140*, 18A301.

(31) Roos, B. O. *Adv. Chem. Phys.*; 1987; pp 399–445.

(32) Andersson, K.; Malmqvist, P. A.; Roos, B. O.; Sadlej, A. J.; Wolinski, K. Second-order perturbation theory with a CASSCF reference function. *J. Chem. Phys. 94*, 5483–5488.

(33) Andersson, K.; Malmqvist, P.-Å.; Roos, B. O. Second-order perturbation theory with a complete active space self-consistent field reference function. *J. Chem. Phys* **1992**, *96*, 1218–1226.

(34) Angeli, C.; Cimiraglia, R.; Evangelisti, S.; Leininger, T.; Malrieu, J.-P. Introduction of n-electron valence states for multireference perturbation theory. *J. Chem. Phys* **2001**, *114*, 10252–10264.

(35) Malček, M.; Vénosová, B.; Puškárová, I.; Kožíšek, J.; Gall, M.; Bučinský, L. Coordination bonding in dicopper and dichromium tetrakis(μ-acetato)-diaqua complexes: Nature, strength, length, and topology. *J. Comput. Chem.* **2019**, *41*, 698–714.

(36) Li, G.; Meng, L.; Zhang, H.; Li, X.; Zeng, Y. Electronic structure of triangular M_3 (M = B, Al, Ga): nonclassical three-center two electron π bond and σ delocalization. *Chem. Chem. Phys.* **2020**, *22*, 18071–18077.

(37) Giricheva, N. I.; Sliznev, V. V.; Alikhanyan, A. S.; Morozova, E. A.; Girichev, G. V. Molecular Structure of Gaseous Oxopivalate Co(II): Electronic States of Various Multiplicities. *Int. J. Mol. Sci.* **2023**, *24*, 13224.

(38) Pech, C. G.; Haase, P. A. B.; Sergentu, D.-C.; Borschevsky, A.; Pilmé, J.; Galland, N.; Maurice, R. Quantum chemical topology at the spin–orbit configuration interaction level: Application to astatine compounds. *J. Comput. Chem.* **2020**, *41*, 2055–2065.

(39) Reuter, L.; Lüchow, A. On the connection between probability density analysis, QTAIM, and VB theory. *Phys. Chem. Chem. Phys.* **2020**, *22*, 25892–25903.

(40) Zhabanov, Y. A.; Sliznev, V. V.; Ryzhov, I. V.; Stuzhin, P. A. Peculiarities of electronic structure and chemical bonding in iron and cobalt metal complexes of porphyrazine and tetra(1, 2, 5-thiadiazole)porphyrazine. *J. Porphyr. Phthalocyanines* **2020**, *24*, 1146–1154.

(41) Pathak, S.; Lang, L.; Neese, F. A dynamic correlation dressed complete active space method: Theory, implementation, and preliminary applications. *J. Chem. Phys* **2017**, *147*.

(42) Fugel, M.; Beckmann, J.; Jayatilaka, D.; Gibbs, G. V.; Grabowsky, S. A Variety of Bond Analysis Methods, One Answer? An Investigation of the Element-Oxygen Bond of Hydroxides H_nXOH. *Eur. J. Chem.* **2018**, *24*, 6248–6261.

(43) Moura Jr., R. T.; Neto, A. N. C.; Malta, O. L.; Longo, R. L. Overlap properties of chemical bonds in generic systems including unusual bonding situations. *J. Mol. Model* **2020**, *26*, 1–18.

(44) Pipek, J.; Mezey, P. G. A fast intrinsic localization procedure applicable for ab-initio and semi-empirical linear combination of atomic orbital wave functions. *J. Chem. Phys.* **1989**, *90*, 4916–4926.

(45) Lehtola, S.; Jónsson, H. Pipek-Mezey Orbital Localization Using Various Partial Charge Estimates. *J. Chem. Theory Comput.* **2014**, *10*, 642–649.

(46) Slater, J. C. The Theory of Complex Spectra. *Phys. Rev.* **1929**, *34*, 1293–1322.

(47) Condon, E. U. The Theory of Complex Spectra. *Phys. Rev.* **1930**, *36*, 1121–1133.

(48) Santos-Jr., C. V.; Lima, E. M.; Moura Jr., R. T. Numerical integration of overlap electron densities: Parallelization strategies for a good load balancing using OpenMP. *Comput Theor Chem* **2021**, *1206*, 113457.

(49) Cremer, D.; Kraka, E. Chemical Bonds without Bonding Electron Density? Does the Difference Electron-Density Analysis Suffice for a Description of the Chemical Bond? *Angew. Chem.* **1984**, *23*, 627–628.

(50) Oliveira, V. P.; Kraka, E.; Machado, F. B. C. Pushing 3c–4e Bonds to the Limit: A Coupled Cluster Study of Stepwise Fluorination of First-Row Atoms. *Inorg. Chem.* **2019**, *58*, 14777–14789.

(51) Pakiari, A.; Eskandari, K. Closed shell oxygen–oxygen bonding interaction based on electron density analysis. *J. Mol. Struct.* **2007**, *806*, 1–7.

(52) Love, I. Polar Covalent Bonds: An AIM Analysis of S, O Bonds. *J. Phys. Chem* **2009**, *113*, 2640–2646.

(53) Farfán, P.; Gómez, S.; Restrepo, A. Dissection of the Mechanism of the Wittig Reaction. *J. Org. Chem* **2019**, *84*, 14644–14658.

(54) Wilson, E. B.; Decius, J. C.; Cross, P. C. M. *Molecular Vibrations. The Theory of Infrared and Raman Vibrational Spectra*; McGraw-Hill: New York, 1955; pp 59–136.

(55) Wilson, E. B. Some Mathematical Methods for the Study of Molecular Vibrations. *J. Chem. Phys.* **1941**, *9*, 76–84.

(56) Konkoli, Z.; Cremer, D. A New Way of Analyzing Vibrational Spectra. I. Derivation of Adiabatic Internal Modes. *Int. J. Quantum Chem.* **1998**, *67*, 1–9.

(57) Konkoli, Z.; Larsson, J. A.; Cremer, D. A New Way of Analyzing Vibrational Spectra. II. Comparison of Internal Mode Frequencies. *Int. J. Quantum Chem.* **1998**, *67*, 11–27.

(58) Kraka, E.; Zou, W.; Tao, Y. Decoding Chemical Information from Vibrational Spectroscopy Data: Local Vibrational Mode Theory. *WIREs: Comput. Mol. Sci.* **2020**, *10*, 1480.

(59) Riplinger, C.; Pinski, P.; Becker, U.; Valeev, E. F.; Neese, F. Sparse maps—A systematic infrastructure for reduced-scaling electronic structure methods. II. Linear scaling domain based pair natural orbital coupled cluster theory. *J. Chem. Phys.* **2016**, *144*.

(60) Riplinger, C.; Neese, F. An efficient and near linear scaling pair natural orbital based local coupled cluster method. *J. Chem. Phys.* **2013**, *138*.

(61) Riplinger, C.; Sandhoefer, B.; Hansen, A.; Neese, F. Natural triple excitations in local coupled cluster calculations with pair natural orbitals. *J. Chem. Phys.* **2013**, *139*.

(62) Rappoport, D.; Furche, F. Property-optimized Gaussian basis sets for molecular response calculations. *J. Chem. Phys.* **2010**, *133*.

(63) Weigend, F.; Furche, F.; Ahlrichs, R. Gaussian basis sets of quadruple zeta valence quality for atoms H–Kr. *J. Chem. Phys.* **2003**, *119*, 12753–12762.

(64) Weigend, F.; Köhn, A.; Hättig, C. Efficient use of the correlation consistent basis sets in resolution of the identity MP2 calculations. *J. Comput. Chem.* **2002**, *116*, 3175–3183.

(65) Gordon, M. S.; Schmidt, M. W.; Chaban, G. M.; Glaesemann, K. R.; Stevens, W. J.; Gonzalez, C. A natural orbital diagnostic for multiconfigurational character in correlated wave functions. *J. Chem. Phys.* **1999**, *110*, 4199–4207.

(66) Neese, F. The ORCA program system. *Comput. Mol. Sci.* **2011**, *2*, 73–78.

(67) Zou, W.; Nori-Shargh, D.; Boggs, J. E. On the Covalent Character of Rare Gas Bonding Interactions: A New Kind of Weak Interaction. *J. Phys. Chem. A* **2012**, *117*, 207–212.

(68) Lu, T.; Chen, F. Multiwfn: A multifunctional wavefunction analyzer. *J. Comput. Chem.* **2011**, *33*, 580–592.

(69) Zou, W.; Moura Jr., R.; Quintano, M.; Bodo, F.; Tao, Y.; Freindorf, M.; Makoś, M. Z.; Verma, N.; Cremer, D.; Kraka, E. LModeA2023. Computational and Theoretical Chemistry Group (CATCO), Southern Methodist University: Dallas, TX, USA, 2023.

(70) Klein, S.; Kochanski, E.; Strich, A.; Sadlej, A. J. Electric properties of the water molecule in 1A1, 1B1, and 3B1 electronic states: Refined CASSCF and CASPT2 calculations. *Theor. Chim. Acta* **1996**, *94*, 75–91.

(71) III, R. D. J. NIST Computational Chemistry Comparison and Benchmark Database NIST Standard Reference Database Number 101 Release 22, May 2022. 2022.

(72) Shaik, S.; Danovich, D.; Silvi, B.; Lauvergnat, D. L.; Hiberty, P. C. Charge-Shift Bonding—A Class of Electron-Pair Bonds That Emerges from Valence Bond Theory and Is Supported by the Electron Localization Function Approach. *Chem. Eur. J.* **2005**, *11*, 6358–6371.

(73) Nottoli, T.; Gauss, J.; Lipparini, F. Second-Order CASSCF Algorithm with the Cholesky Decomposition of the Two-Electron Integrals. *J. Chem. Theory Comput.* **2021**, *17*, 6819–6831.

(74) Bent, H. A. An Appraisal of Valence-bond Structures and Hybridization in Compounds of the First-row Elements. *Chem. Rev.* **1961**, *61*, 275–311.

(75) Alabugin, I. V.; Bresch, S.; Manoharan, M. Hybridization Trends for Main Group Elements and Expanding the Bent's Rule Beyond Carbon: More

than Electronegativity. *J. Phys. Chem. A* **2014**, *118*, 3663–3677.

(76) Sivalingam, K.; Krupicka, M.; Auer, A. A.; Neese, F. Comparison of fully internally and strongly contracted multireference configuration interaction procedures. *J. Chem. Phys.* **2016**, *145*, 054104.

(77) Bauschlicher, J., Charles W.; Langhoff, S. R. Full configuration-interaction study of the ionic–neutral curve crossing in LiF. *J. Chem. Phys.* **1988**, *89*, 4246–4254.

TOC Graphic

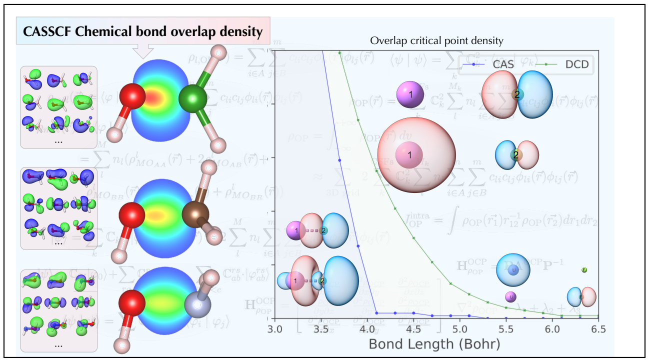
CASSCF Chemical bond overlap density
Overlap critical point density
CAS
DCD
1
2
3.0
3.5
4.0
4.5
5.0
5.5
6.0
6.5
Bond Length (Bohr)